5G-Compliant Integrated Sensing and Communication at Sub-6 GHz: Experiments with SDRs and OpenAirInterface

Salvatore Carbonara*†, Daniele Pugliese*†, Alessio Fascista*†, Angelo Coluccia‡†, Gennaro Boggia*†

*Dept. of Electrical and Information Engineering, Politecnico di Bari, Bari, Italy;
‡Department of Engineering, Università del Salento, Lecce, Italy;
†CNIT, Consorzio Nazionale Interuniversitario per le Telecomunicazioni.

***Abstract*—Integrated Sensing and Communication (ISAC) is attracting significant interest, with numerous studies highlighting its potential in 5G and beyond. Unfortunately, due to the inherent difficulty in integrating ISAC into non-proprietary hardware and software platforms, experimental works remain few and mainly focused on the use of 5G NR-like waveforms (often within simulated environments), lacking a 5G-compliant protocol stack enabling an end-to-end network connectivity. In this work, we present an experimental testbed for monostatic ISAC based on Software Defined Radios (SDRs) and OpenAirInterface (OAI), an open-source 5G framework adhering to the 3GPP standard. In addition to a description of the main implementation details, we present a fully digital signal processing pipeline which utilizes downlink slots of a 5G OFDM-based communication in the sub-6 GHz n77 band to enable ISAC capabilities at the 5G Node B. In the first phase, processing steps include temporal alignment of the TX and RX I/Q samples, compensating for the processing delays introduced by the OAI framework and SDR platforms. Then, after dealing with the lack of TX–RX isolation and associated Self-Interference (SI) through fully digital mitigation techniques, the digitized signals are processed using either a Matched Filter or Channel Estimation-like scheme. Experimental evaluations conducted in a cluttered indoor environment under controlled target conditions show promising capabilities in estimating both range and velocity of targets, also highlighting notable trade-offs arising from the presence of side-lobes in the range-Doppler maps, linked to residual SI and use of 5G communication signals.**

***Index Terms*—Integrated Communication and Sensing, OpenAirInterface, Software-Defined Radio, 5G, range-Doppler maps**

I. INTRODUCTION

Integrated Sensing and Communication (ISAC) has emerged as a key enabler in Fifth Generation (5G) and beyond, allowing joint sensing and communication over shared spectral and hardware resources [1]–[3]. This integration supports diverse applications such as autonomous driving, smart cities, and remote healthcare [4], [5]. Recent works have addressed ISAC design principles and challenges, emphasizing the trade-offs between sensing and communication [6], the role of advanced technologies as reconfigurable intelligent surfaces [7], and the need for robust signal processing and optimization [8]–[10].

On the other hand, experimental evaluation of ISAC remains a complex task, mainly due to the difficulty in integrating ISAC into non-proprietary hardware and dedicated software that manage protocol stack operations. Most existing works indeed rely on simulations or synthetic 5G-like OFDM waveforms [11]–[17]. For instance, [11] investigates a bistatic mmWave scenario where 5G-mimicking signals are classified via a deep neural network. Monostatic testbeds operating at mmWave frequencies with 5G-like frame structures are explored in [12], [13], though the former uses non-standard frequency bands, and the latter focuses primarily on crosstalk mitigation. At sub-6 GHz, [14] assessed sensing feasibility using only the 5G Synchronization Signal Block (SSB), while [15] provided a thorough analysis of sensing based on 5G, introducing a new circuitry for Self-Interference (SI) mitigation and presenting experimental results with synthetic signals. The SI mitigation is required because 5G systems use time slots as the shortest TX duration. Typical scatterer delays (e.g., 50–300 ns indoors) are shorter than a slot, requiring the gNB to perform simultaneous TX/RX with limited channel isolation, which produces strong SI that can mask weaker target echoes at short ranges [18]. Finally, [16], [17] also adopt synthetic sub-6 GHz waveforms, but not in standard-compliant settings.

In this work, we present a 5G-compliant experimental testbed for monostatic ISAC based on the OpenAirInterface (OAI) framework, operating in the sub-6 GHz band. Leveraging commercial Software Defined Radios (SDRs) and a OAI 5G Node B (gNB) in a Standalone (SA) configuration, we demonstrate the feasibility of reusing actual 5G communication signals to sense both moving and static objects near the gNB, within the ISAC paradigm. A fully digital signal processing pipeline is developed to extract range-Doppler maps from the RX signals, incorporating compensation for temporal misalignments and mitigation of SI. Experimental evaluations in a cluttered indoor environment confirm the possibility to estimate target range and velocity using sub-6 GHz 5G communication signals, while highlighting key trade-offs when sensing both static and dynamic targets.

II. 5G PHYSICAL LAYER, SIGNAL MODELS, AND SENSING PROCESSING

A. 5G NR Physical Layer

The 3rd Generation Partnership Project (3GPP) standardization of 5G introduced key enhancements over Long Term Evolution (LTE), redefining the Next Generation Radio Access Network (NG-RAN). As in LTE, 5G employs OFDM, now extended to both downlink and uplink, which can be scheduled on a single element of the so-called 5G *resource grid* spanning the time and frequency domains. Each cell operates on at least one BandWidth Part (BWP), partitioned into multiple

Resource Blocks (RBs) each comprising 12 contiguous OFDM subcarriers. A transmission is organized into frames of duration $10\,\mathrm{ms}$, subdivided into slots, each conveying a sequence of 14 OFDM symbols [19]. Let f_{carrier} denote the carrier frequency of the considered BWP, and N_{RB} the number of allocated RBs. To support a wide range of services, the 5G New Radio (NR) introduces a flexible numerology framework, parameterized by μ, which impacts both spectral granularity and transmission latency. Specifically, $\Delta f = 2^{\mu} \cdot 15 \quad [\text{kHz}]$, $T_{\text{slot}} = 14T_{\text{symb}} = \frac{1}{2^{\mu}} \quad [\text{ms}]$, and $T_{\text{symb}} = 1/\Delta f + T_{\text{CP}}$ denote Subcarrier Spacing (SCS), slot duration, and OFDM symbol duration, respectively, with T_{CP} the Cyclic Prefix (CP) duration, and $\mu \in \{0, \ldots, 6\}$. Thus, a larger numerology index μ yields a wider SCS and reduced symbol and slot durations, allowing for lower transmission latencies. Consequently, the number of time slots per frame, denoted as S_{μ}, increases with μ. The applicable values of μ depend on the operational frequency range: for Frequency Range 1 (FR1), corresponding to sub-6 GHz bands, the 3GPP standard allows $\Delta f \leq 60\,\text{kHz}$, while for Frequency Range 2 (FR2), which encompasses millimeter-wave (mmWave) frequencies, only numerologies with $\Delta f \geq 60\,\text{kHz}$ are permitted. This work focuses on sub-6 GHz FR1 deployments, where the maximum bandwidth is $100\,\text{MHz}$, translating into $24 \leq N_{\text{RB}} \leq 275$.

TX Signal Model: We denote the 5G NR resource grid at the TX side as $\boldsymbol{X} \in \mathbb{C}^{S \times M}$, where $m = 1, \ldots, M$ indexes the OFDM symbols along the time domain, and $s = 1, \ldots, S$ indexes the subcarriers. According to the frame structure recalled above, $\boldsymbol{X}$ is a complex-valued matrix consisting of $S = 12N_{\text{RB}}$ rows and $M = 14S_{\mu}$ columns. Before being transmitted through the gNB TX channel, $\boldsymbol{X}$ undergoes (i) an Inverse Fast Fourier Transform (IFFT) to map subcarriers samples to I/Q samples (time domain), (ii) the insertion of the CP, and (iii) feeding the I/Q samples to a Digital-to-Analog Converter (DAC) to reconstruct the (baseband) signal to be transmitted. The time-domain waveform corresponding to the m-th column (OFDM symbol) of $\boldsymbol{X}$ is

$$x_m(t) = \sum_{s=1}^{S} [\boldsymbol{X}]_{s,m} e^{j2\pi(s - S_{\text{off}})\Delta f (t+T)}, \tag{1}$$

with T either $(T_{\text{symb}} - T_{\text{CP}})$ for $t \in [0, T_{\text{CP}})$ or $T = -T_{\text{CP}}$ for $t \in [T_{CP}, T_s]$, $S_{\text{off}} = \left\lfloor \frac{S}{2} \right\rfloor + 1$ is the offset (in subcarriers) introduced to align the subcarrier index, the latter spanning $[-\lfloor S/2 \rfloor, \lfloor S/2 \rfloor - 1]$, with the row indices s of the matrix.

It is important to note that, differently from experiments with generated 5G-like waveforms, in a 5G-compliant full stack setup the structure of $\boldsymbol{X}$ is not controllable, as it is determined by two factors: the dynamic resource allocation strategy adopted by the network for control and data channels, and the specific duplexing scheme in use. As a result, it becomes infeasible to guarantee the use of fixed and repeatable $\boldsymbol{X}$ for ISAC purposes (e.g., calibration or reference).

RX Signal Model: The signal received at the gNB RX channel undergoes the reverse processing chain, i.e., analog-to-digital conversion (ADC), CP removal and Fast Fourier Transform (FFT), yielding the received resource grid $\boldsymbol{Y} \in \mathbb{C}^{S \times M}$. Generally, the entries of $\boldsymbol{Y}$ result from the superposition of an undesired link between the TX and RX channels on the gNB, due to the lack of perfect isolation and causing the SI, and multiple delayed and attenuated replicas of the TX signal caused by reflections from the environment. Specifically, the (s, m)-th entry of $\boldsymbol{Y}$ can be expressed as

$$[\boldsymbol{Y}]_{s,m} = [\boldsymbol{Y}]^{\text{SI}}_{s,m} + \sum_{i=1}^{N_{\text{scat}}} \alpha_i [\boldsymbol{X}]_{s,m} e^{j2\pi(mT_{\text{symb}} f_i - s\Delta f \tau_i)} + w_{s,m},$$

where α_i, f_i, τ_i represent the attenuation factor, Doppler shift and delay associated with the reflection from the i-th scatterer, respectively, N_{scat} is the number of dominant scatterers, and $w_{s,m}$ a random variable capturing the disturbance contributions. As to $[\boldsymbol{Y}]^{\text{SI}}_{s,m}$, it represents the SI contribution between TX and RX channels; in Sec. II-C, we will discuss fully digital techniques that can be adopted to mitigate its impact.

B. Monostatic ISAC Processing

Following a monostatic ISAC paradigm [20], $\boldsymbol{X}$ and $\boldsymbol{Y}$ can be processed at the gNB to estimate $\{f_i\}_{i=1}^{N_{\text{scat}}}$ and $\{\tau_i\}_{i=1}^{N_{\text{scat}}}$, which are then mapped to range and velocity information. In particular, range and velocity can be estimated by analyzing the so-called radar image (or range–Doppler profile) obtained via the 2D periodogram $\boldsymbol{P}$, whose elements are [21]

$$[\boldsymbol{P}]_{v,r} = \left| \sum_{m=0}^{\tilde{M}-1} \left(\sum_{s=0}^{\tilde{S}-1} [\boldsymbol{F}]_{s,m} [\boldsymbol{W}]_{s,m} e^{j2\pi \frac{sv}{\tilde{S}}} \right) e^{-j2\pi \frac{mr}{\tilde{M}}} \right|^2, \tag{2}$$

where v and r denote the velocity and range bin indices, $\boldsymbol{F}$ is the matrix resulting from the joint processing of $\boldsymbol{X}$ and $\boldsymbol{Y}$, $\tilde{S} \geq S$ and $\tilde{M} \geq M$ are the size of the inner IFFT (range profiles) and outer FFT (velocity profiles), and $\boldsymbol{W}$ a windowing matrix. As to $\boldsymbol{F}$, we consider two alternative processing strategies, i.e., *Matched Filter (MF)* and *Channel Estimation-like (CH)* [15]. In the MF case, we perform $\boldsymbol{F}^{\text{MF}} = \boldsymbol{Y} \odot \boldsymbol{X}^*$, with $\odot$ the Hadamard (element-wise) product and $(\cdot)^*$ the complex conjugate operator, obtaining

$$[\boldsymbol{F}^{\text{MF}}]_{s,m} = \sum_{i=1}^{N_{\text{scat}}} \alpha_i \left| [\boldsymbol{X}]_{s,m} \right|^2 e^{j2\pi(mT_{\text{symb}} f_i - s\Delta f \tau_i)} + w^{\text{MF}}_{s,m}, \tag{3}$$

where $w^{\text{MF}}_{s,m}$ is the noise contribution after MF processing. In the CH case, denoting by $\oslash$ the element-wise division, $\boldsymbol{F}^{\text{CH}} = \boldsymbol{Y} \oslash \boldsymbol{X}$ with entries given by

$$[\boldsymbol{F}^{\text{CH}}]_{s,m} = \sum_{i=1}^{N_{\text{scat}}} \alpha_i e^{j2\pi(mT_{\text{symb}} f_i - s\Delta f \tau_i)} + w^{\text{CH}}_{s,m}, \tag{4}$$

and $w^{\text{CH}}_{s,m}$ is the noise contribution after CH processing.

The associated range and velocity parameters $\{(R_i, V_i)\}_{i=1}^{N_{\text{scat}}}$, expressed in m and $\mathrm{m/s}$, respectively, can be estimated by identifying the N_{scat} dominant peaks in the range-velocity profile $\boldsymbol{P}$. For clarity of exposition, we consider $N_{\text{scat}} = 1$. Under this assumption, the peak location of $\boldsymbol{P}$ corresponds to the Maximum Likelihood (ML) estimate of the target range and velocity $(\hat{R}^{\text{ML}}_1, \hat{V}^{\text{ML}}_1) = \arg\max_{v,r} [\boldsymbol{P}]_{v,r}$ [21]. We note that the resolution in the range–velocity profile $\boldsymbol{P}$ (assuming $\tilde{S} = S$ and $\tilde{M} = M$) is inherently tied to the number of subcarriers and OFDM symbols processed in the frequency domain as $\Delta r = c/(2S\Delta f)$ and $\Delta v = c/(2MT_{\text{symb}}f_{\text{carrier}})$, with c the speed of light. It is important to consider that the structure of $\boldsymbol{X}$ in a practical 5G-compliant system exhibits substantial variability, both in terms of subcarrier occupancy and active OFDM symbols within a radio frame. This variability arises from the dynamic allocation of physical channels and signals (e.g., PSS, SSS, PDSCH, PDCCH, ...), which are scheduled adaptively based on traffic demands and quality-of-service requirements. Moreover, downlink transmissions are interspersed with periods reserved for uplink access, during which the gNB ceases transmission and listens for incoming signals (e.g., sounding reference signals or random access requests). Consequently, the resulting $\boldsymbol{X}$ is typically sparse, fragmented, and time-varying, with such irregularity directly affecting the achievable range and velocity resolution, and posing additional challenges for ISAC processing.

C. Digital SI Mitigation Algorithm

SI mitigation typically relies on a combination of passive suppression, RF analog cancellation, and digital cancellation techniques [22]. Passive suppression reduces SI via physical isolation, e.g., spatial separation, highly-directive and shielded antennas (e.g., horn antennas), and optimized placement [23]. RF analog cancellation introduces controlled destructive interference before reception [15], while digital cancellation mitigates SI via signal processing in the digital domain [24]. Although highly effective, RF cancellers generally require additional dedicated hardware, often beyond the capabilities of standard communication prototypes.

In this work, our aim is to perform ISAC relying solely on a minimal hardware and software required for a 5G-compliant communication system, and thus consider only digital cancellation algorithms and a very simple passive suppression for mitigating SI. As detailed in Sec. III, passive suppression only consists in using commercial off-the-shelf log-periodic antennas, whose higher directivity helps to attenuate the signals from the TX to the RX ports. Regarding the SI digital mitigation, we adopt adaptive strategies that try to approximate the actual nonlinear input–output relationship of the SI channel via a linear combination of suitably chosen basis functions [25]. Specifically, let $x[n]$ denote the digital I/Q samples of the M symbols that constitute the TX waveform for $m = 1, \ldots, M$, and $\psi_p(x[n])$ a p-th order non-linear basis function, with $p \in \{\mathbb{N} \mid 1 \leq p \leq P, p \text{ odd}\}$. Even terms are not considered because they generate spectral components far from f_{carrier} [26]. The resulting digital SI contribution is then modeled as

$$y^{\text{SI}}[n] = \sum_{p=1, p \text{ odd}}^{P} \sum_{k=0}^{K-1} h_p^*[k]\psi_p(x[n-k]), \tag{5}$$

with $\boldsymbol{h}_p = [h_p[0] \ \cdots \ h_p[K-1]]^{\mathsf{T}} \in \mathbb{C}^{K\times 1}$ coefficients of the SI channel response for each p-order basis and K is the memory of the filter. To mitigate the SI, we need to estimate $y^{\text{SI}}[n]$ and subtract it from the digital RX signal as

$$\tilde{y}[n] = y[n] - \sum_{p=1,\, p \text{ odd}}^{P} \hat{\boldsymbol{h}}_p^{\mathsf{H}} \boldsymbol{u}_p[n], \tag{6}$$

with $\hat{\boldsymbol{h}}_p = [\hat{h}_p[0] \ \cdots \ \hat{h}_p[K-1]]^T \in \mathbb{C}^{K\times 1}$ the estimated filter parameters for the p-th order input signal and $\boldsymbol{u}_p[n] = [\psi_p(x[n]) \ \cdots \ \psi_p(x[n-K])]^T \in \mathbb{C}^{K\times 1}$. Following [25], we adopt an iterative Least Mean Squares (LMS) algorithm using Hammerstein Polynomials (HP) as basis functions, i.e., $\psi_p(x[n]) = \left|x[n]^{p-1}\right| x[n]$. Specifically, we initialize $\hat{\boldsymbol{h}}_p$ as a zero vector and estimate $\hat{\boldsymbol{h}}_p$ according to the update rule

$$\hat{\boldsymbol{h}}_p \leftarrow \hat{\boldsymbol{h}}_p + \eta \ \tilde{y}^*[n]\boldsymbol{u}_p[n], \tag{7}$$

where η is the learning rate of the canceller. The update rule is applied iteratively for each sample of the TX signal $x[n]$ to refine the estimate of $\hat{y}^{\text{SI}}[n]$, resulting in a new post-processed signal $\tilde{y}[n]$ where the SI is progressively mitigated. It is important to note that the choice of K must be made carefully, as it is related to the minimum detectable range for static targets: indeed, reflections with delays within this window are interpreted as part of the SI and thus suppressed. This trade-off will be further examined in Sec. IV.

III. EXPERIMENTAL TESTBED FOR 5G-COMPLIANT ISAC

A global overview of the proposed 5G-compliant ISAC experimental testbed is provided in Fig. 1, where the left side illustrates the *Software Framework*, comprising the *User* and the *Communication & Sensing* subsystems, while the right side shows the *Hardware setup*. Details are given below.

A. Hardware Setup

The proposed testbed is built on top of the SDR NI Ettus USRP X410, for the User Equipment (UE) and the gNB. The former mounts VERT2450 antennas for both TX and RX channels, which present an almost omnidirectional gain along the horizontal plane. For the latter, we have chosen LP0965 log-periodic PCB antennas — placed apart from the SDR using $1\,\mathrm{m}$ long Radio Frequency (RF) cables — which provide $\sim 6\,\mathrm{dBi}$ gain, to partially mitigate the contribution of SI in a passive way. Moreover, to ensure a more stable connectivity, an OctoClock-G CDA-2990 broadcasts precise reference signals to synchronize the SDRs. Note that this does not affect the sensing performance, i.e., the testbed can operate even without such a device. Regarding the computing resources, our setup includes two Ubuntu 24.04 LTS workstations, each equipped with an AMD Ryzen Threadripper PRO 5965WX processor, 128 GB of DDR4 RAM. As shown on the right side of Fig. 1, the workstation WS-0 hosts the gNB performing the ISAC process, while the UE stack is executed on WS-1. Each workstation controls its SDR via a 4xSFP28 to QSFP28 connection, enabling a high-speed link up to $100\,\mathrm{Gbps}$.

B. Communication Subsystem

For the communication components of the Software Framework, we adopt the open-source 5G network implementation provided by the OAI Software Alliance, i.e., OpenAirInterface5G [27]. The Communication Subsystem relies on the OAI Core Network (CN), which provides the essential network functions for 5G operations — namely, the User

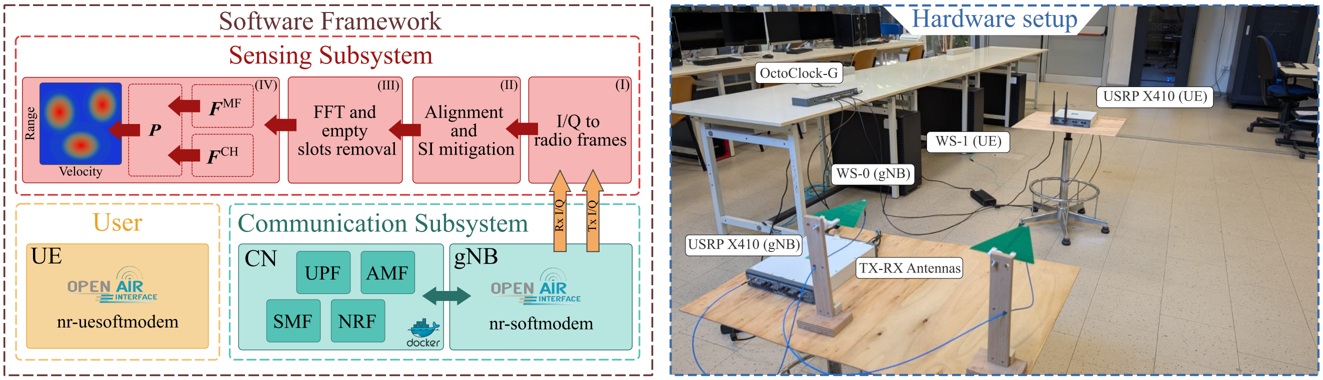

Fig. 1. Comprehensive representation of the proposed 5G-compliant ISAC testbed, including the main software (left) and hardware (right) components.

Plane Function (UPF), Access and Mobility Management Function (AMF), Session Management Function (SMF), and Network Repository Function (NRF), as shown in Fig. 1. All components are deployed as Docker containers using official OAI images. Besides the CN, the workstation WS-0 hosts the protocol stack implementation of the gNB provided by OAI. All the functionalities performed by the gNB are implemented by means of the executable `nr-softmodem`. Additionally, we appended the flags `--T_stdout 2 --T_nowait` to the execution command to enable extensive low-level data logging via the *T_tracer* utility [27], from which we specifically extracted the I/Q samples transmitted and received by the gNB. Note that this utility does not add any overhead to the ongoing data transmissions. Similarly, the UE protocol stack is launched on WS-1 using the `nr-uesoftmodem` executable.

C. Sensing Subsystem

The Sensing Subsystem can retrieve I/Q samples transmitted and received between the users. To this aim, the T_tracer command `record` is exploited, specifying the parameters `-OFF -on USRP_TX_ANT0 -on USRP_RX_ANT0` to explicitly activate the recording of transmitted and received I/Q samples, i.e., $x[n]$ and $y[n]$. These are then processed as follows.

(I) I/Q to radio frames: We organize I/Q samples into $10\,\mathrm{ms}$ chunks, according to the associated timestamps, which correspond to 5G radio frames. It should be noted that the TX signal traces present empty intervals in correspondence to uplink phases, which are filled with zero values in this step.

(II) Alignment and SI mitigation: The RX frames are delayed from the TX ones by a few µs, due to latency of the software/hardware processing. This offset is estimated via peak correlation and compensated accordingly. Subsequently, SI is estimated and mitigated using the algorithm from Sec. II-C

(III) FFT and empty slots removal: By performing the CP removal and FFT on the I/Q samples, $\boldsymbol{X}$ and $\boldsymbol{Y}$ are retrieved. We exclude the columns in which the gNB does not transmit, as they do not add any information in the calculation of $\boldsymbol{F}$. This produces a resource grid with fewer symbols, which directly impacts the resolution Δv.

(IV) Computation of $\boldsymbol{F}$ and $\boldsymbol{P}$: We finally compute $\boldsymbol{F}^{\mathrm{MF}}$ or $\boldsymbol{F}^{\mathrm{CH}}$ according to (3) or (4), respectively, which in turn yield the range-Doppler maps $\boldsymbol{P}$ as defined in (2).

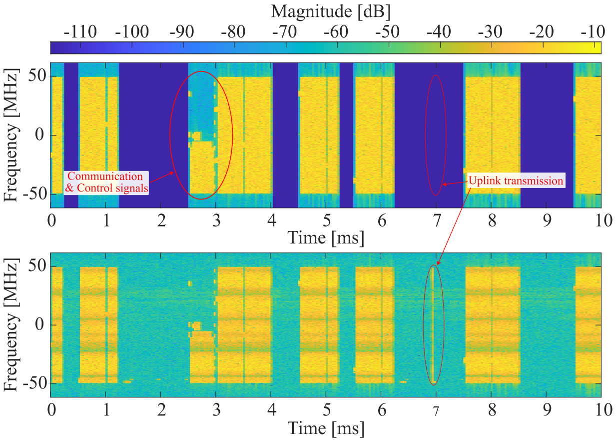

Fig. 2. Examples of the spectrograms of the TX (top) and RX (bottom) 5G NR radio frames at the gNB.

IV. EXPERIMENTAL RESULTS

Our measurement campaign is conducted within an indoor laboratory environment of approximately $100\,\mathrm{m}^2$, by placing the gNB and the UE approximately $2\,\mathrm{m}$ apart, with the two gNB antennas spaced by $40\,\mathrm{cm}$. The cell was configured with $f_{\text{carrier}} = 3.995\,\mathrm{GHz}$, assigned by the Italian government for academic experimentation, which falls within the n77 band (FR1, sub-6 GHz), a subcarrier spacing $\Delta f = 30\,\mathrm{kHz}$, and a total signal bandwidth $B = 100\,\mathrm{MHz}$, corresponding to $N_{\mathrm{RB}} = 273$ resource blocks (i.e., $S = 3276$ subcarriers). These configurations enable experiments compatible with the 5G Standalone (SA) operation. Once the UE is connected to the network, we initiate a downlink transmission from the gNB using the `iperf3` utility, while the uplink is limited to control signaling from the UE. This is essential to ensure that the full bandwidth is used, hence giving insights on the achievable sensing performance when communication is simultaneously performed, i.e., the same 5G-compliant waveform is exploited for ISAC. All I/Q samples were captured at a sampling frequency $f_{\text{samp}} = 122.88\,\mathrm{MHz}$ for subsequent processing.

Fig. 2 shows the spectrograms of the TX (top) and RX (bottom) 5G NR radio frames at the gNB, generated by the OAI protocol stack. Blue stripes in the TX spectrogram corre-

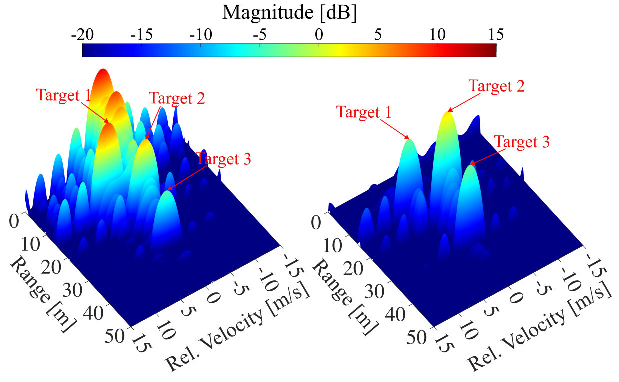

(a) (b)

Fig. 3. 3D range-Doppler maps of $\boldsymbol{F}^{\text{CH}}$ with (a) no SI mitigation and (b) SI mitigation with $K = 15$, with the three visible targets.

spond to inactive symbols or uplink time slots; accordingly, the RX spectrogram primarily shows background noise in these intervals, except when the UE actively transmits, as visible for instance around $7\,\text{ms}$. Similarly, the light-blue stripes in the TX spectrogram correspond to inactive subcarriers within active symbols, but they are not visible in the RX spectrogram as they are buried in the noise floor. The presence of additional control downlink signals (e.g., SSB) is visible in the TX spectrogram (e.g. between 2.5 and 3 ms) where only a portion of the available bandwidth is utilized. As discussed in Sec. III-C, we discard symbols where no communication occurs; since this reduces the Doppler resolution, two consecutive radio frames are processed for an overall $20\,\text{ms}$ signal.

To ascertain the sensing capability for different types of static and dynamic targets within the cluttered experimental environment of Fig. 1 and to overcome both the TX power limits and the laboratory size constraints, which hinder the generation of fast-moving targets, we synthetically add N_{target} target returns in the received signal, i.e., $y[n]+\sum_{q=1}^{N_{\text{target}}} \alpha_q x[n-\tau_q]e^{j2\pi n\frac{f_q}{f_{\text{samp}}}}$, where τ_q is the delay in samples of the signal backscattered from target q, and $f_q = 2V_q f_{\text{carrier}}/c$ is the Doppler shift induced by the relative target radial velocity V_q. Finally, the attenuation parameter α_q is computed by setting a controlled signal-to-noise ratio SNR_q for the signal backscattered by the q-th target, then inverting the relation as $\alpha_q^2 = \text{SNR}_q \frac{P_{\text{RX}}}{P_{\text{TX}}}$, with P_{TX} and P_{RX} the average TX and RX powers computed from $y[n]$ and $x[n]$. After determining α_q, we use the radar equation to compute the corresponding range R_q, then obtain the associated τ_q in samples by converting the round-trip delay via the sampling frequency f_{samp}.

For the sake of the analysis, we generate three targets with $\text{SNR}_1 = -6$ dB, $\text{SNR}_2 = -12$ dB and $\text{SNR}_3 = -20$ dB, with the first being a dynamic target moving with velocity $V_1 = 5$, while the other two are static, i.e., $V_2 = V_3 = 0$, at ranges $R_1 = 14, R_2 = 20, R_3 = 31$, respectively. Fig. 3 reports the range-Doppler maps for the $\boldsymbol{F}^{\text{CH}}$ processing scheme, before (left) and after (right) mitigation of the SI, using the algorithm in Sec. II-C. As evident from Fig. 3(a), the region around zero velocity and up to approximately 15 meters in range exhibits multiple peaks, primarily due to the impact of the SI and strong clutter returns from the environment, making identification of static targets very challenging. After applying the SI mitigation algorithm with $K = 15$, $P = 11$, and $\eta = 10^{-3}$, Fig. 3(b) shows that most of the peaks in the low-range, zero-velocity region are effectively suppressed. Notably, target 1 remains visible, albeit with reduced magnitude, due to its dynamic nature, which differentiates it from the SI and clutter components. On the other hand, targets 2 and 3, although static, remain unaffected by the SI mitigation algorithm due to their greater distances, an aspect better clarified in the following.

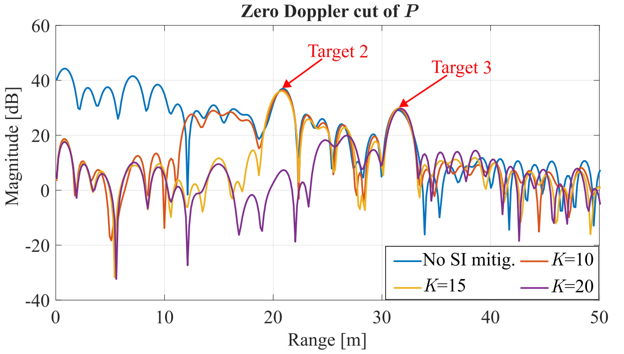

Fig. 4. Zero-Doppler cut (range profiles) of the range-Doppler map for different values of K compared with the case without SI mitigation.

We investigate the impact of the SI mitigation filter memory K by examining in Fig. 4 the zero-Doppler cut of the range-Doppler map. We compare the range profiles with and without SI mitigation, for increasing values of $K \in \{10, 15, 20\}$. It is apparent that increasing K enhances the ability to suppress SI and clutter over progressively larger ranges. Thus, this parameter must be carefully tuned, as overly high values of K can inadvertently suppress legitimate target reflections. This is the case of $K = 20$ in Fig. 4, where the peak corresponding to target 2 is completely suppressed, because target 2 falls within the memory window of the SI mitigation filter: indeed, the latter cancels contributions from ranges up to approximately $\frac{c}{2} \cdot \frac{K}{f_s}$ which, for $K = 20$, corresponds to about 25 meters, and target 2 is at $R_2 = 20$. For the same reason, the peak associated to target 3 at $R_3 = 31$ remains clearly visible. This highlights a fundamental trade-off between effectiveness of SI mitigation and a minimum detectable range for static targets.

To conclude the analysis, Fig. 5 presents a comparison between the range-Doppler maps obtained using the $\boldsymbol{F}^{\text{MF}}$ and $\boldsymbol{F}^{\text{CH}}$ processing, both after SI mitigation with $K = 15$. Both processing schemes allow to reliably identify targets and estimate their range and relative velocity, even in harsh cluttered environments, with the $\boldsymbol{F}^{\text{CH}}$ exhibiting slightly lower sidelobe levels. These findings confirm the feasibility of exploiting sub-6 GHz 5G communication signals for ISAC applications.

V. CONCLUSION

We presented a 5G-compliant monostatic ISAC testbed based on SDRs and the OAI framework, operating in the sub-6 GHz band. A fully digital processing pipeline was developed,

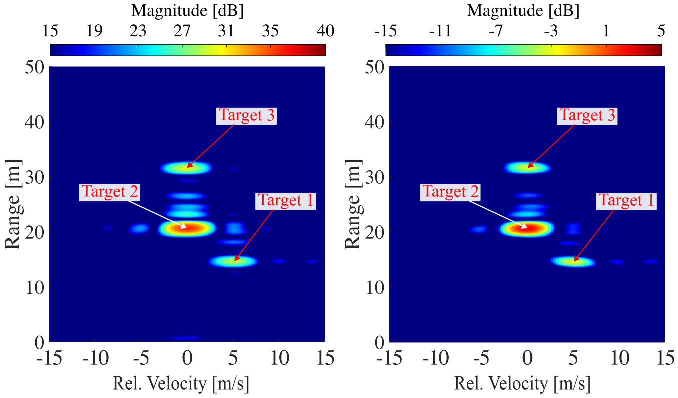

(a) (b)

Fig. 5. Comparison of range-Doppler maps obtained with (a) $\boldsymbol{F}^{\mathrm{MF}}$ and (b) $\boldsymbol{F}^{\mathrm{CH}}$ processing schemes, with $K = 15$.

featuring temporal alignment and self-interference mitigation without requiring specialized hardware. Downlink 5G signals were processed using matched filter and channel estimation-like methods alongside classical periodogram techniques. Experimental results from a cluttered indoor environment, shown via range-Doppler maps and zero-Doppler profiles, demonstrate that sub-6 GHz 5G signals can effectively support sensing, paving the way for native ISAC integration into 5G systems without significant hardware/software modifications. Future work will focus on evaluating detection performance across different SNR conditions using adaptive algorithms able to cope with multiple targets. In addition, to overcome the SDR transmit power and laboratory size limitations, outdoor field experiments will be conducted using real targets.

ACKNOWLEDGEMENTS

This work was supported by the EU under Italy NRRP (NextGenerationEU): RESTART (PE00000001, CUP: D93C22000910001), MOST (CN00000023, CUP: D93C22000410001), and SERICS (PE00000007, CUP: D33C22001300002, project ISP5G+). Additional support came from PRIN 2022 projects INSPIRE (2022BEXMXN 01) and HORUS (2022P44KA8) funded by MUR, and the HORIZON MSCA project BRIDGITISE (grant 101119554).

REFERENCES

[1] X. Luo, Q. Lin, R. Zhang, H.-H. Chen, X. Wang, and M. Huang, "ISAC – A Survey on Its Layered Architecture, Technologies, Standardizations, Prototypes and Testbeds," *IEEE Comm. Surveys & Tut.*, pp. 1–1, 2025.

[2] N. González-Prelcic, D. Tagliaferri, M. F. Keskin, H. Wymeersch, and L. Song, "Six Integration Avenues for ISAC in 6G and Beyond," *IEEE Vehicular Technology Magazine*, vol. 20, no. 1, pp. 18–39, 2025.

[3] F. Matera, M. Settembre, A. Rago, A. Fascista, G. Piro, L. A. Grieco, F. Malandrino, G. Virone, E. Cianca, M. Ruggieri, and S. Morosi, "Terrestrial and Non-Terrestrial Networks for Integrated Sensing and Communication," in *2024 IEEE International Symposium on Systems Engineering (ISSE)*, 2024, pp. 1–5.

[4] A. Liu, Z. Huang, M. Li, Y. Wan, W. Li, T. X. Han, C. Liu, R. Du, D. K. P. Tan, J. Lu, Y. Shen, F. Colone, and K. Chetty, "A Survey on Fundamental Limits of Integrated Sensing and Communication," *IEEE Comm. Surveys & Tutorials*, vol. 24, no. 2, pp. 994–1034, 2022.

[5] X. Li, Y. Cui, J. A. Zhang, F. Liu, D. Zhang, and L. Hanzo, "Integrated Human Activity Sensing and Communications," *IEEE Communications Magazine*, vol. 61, no. 5, pp. 90–96, 2023.

[6] Y. Liu, M. Li, A. Liu, J. Lu, and T. X. Han, "Information-Theoretic Limits of Integrated Sensing and Communication With Correlated Sensing and Channel States for Vehicular Networks," *IEEE Transactions on Vehicular Technology*, vol. 71, no. 9, pp. 10 161–10 166, 2022.

[7] M. I. Ismail, A. M. Shaheen, M. M. Fouda, and A. S. Alwakeel, "RIS-Assisted Integrated Sensing and Communication Systems: Joint Reflection and Beamforming Design," *IEEE Open Journal of the Communications Society*, vol. 5, pp. 908–927, 2024.

[8] Z. Wei, H. Qu, L. Ma, and C. Pan, "Robust ISAC Signal Processing on Unlicensed Spectrum Bands," in *2022 IEEE/CIC International Conference on Communications in China*, 2022, pp. 117–121.

[9] A. Coluccia and A. Fascista, "Energy Threshold Setting With Bounded Performance for Sensing and Communications Under the η-μ Model," in *2023 IEEE International Workshop on Technologies for Defense and Security (TechDefense)*, 2023, pp. 346–351.

[10] A. Coluccia and A. Fascista, "Low-Complexity Prediction of Energy Statistic Exceedance Probability for η-μ Variates," *IEEE Signal Processing Letters*, vol. 31, pp. 3094–3098, 2024.

[11] A. Paidimarri, A. Tzadok, S. G. Sanchez, A. Kludze, A. Gallyas-Sanhueza, and A. Valdes-Garcia, "Eye-Beam: A mmWave 5G-compliant platform for integrated communications and sensing enabling AI-based object recognition," *IEEE Journ. on Selected Areas in Comm.*, 2024.

[12] N. Maletic, M. Petri, M. Appel, and E. Grass, "A Software-Defined Radio Solution for Integrated mmWAVE Communication and Sensing," in *2025 IEEE Wireless Communications and Networking Conference (WCNC)*. IEEE, 2025, pp. 1–6.

[13] B. Duan, T. Li, W. Pan, H. Zhou, Y. Shen, Y. Liu, and S. Shao, "In-Band Full-Duplex Communication for OFDM Integrated Sensing and Communication Systems," *IEEE Internet of Things Journal*, 2025.

[14] M. Golzadeh, E. Tiirola, L. Anttila, J. Talvitie, K. Hooli, O. Tervo, I. Peruga, S. Hakola, and M. Valkama, "Downlink Sensing in 5G-Advanced and 6G:SIB1-assisted SSB Approach," in *2023 IEEE 97th Vehicular Technology Conference (VTC2023-Spring)*, 2023, pp. 1–7.

[15] C. Baquero Barneto, T. Riihonen, M. Turunen, L. Anttila, M. Fleischer, K. Stadius, J. Ryynänen, and M. Valkama, "Full-Duplex OFDM Radar With LTE and 5G NR Waveforms: Challenges, Solutions, and Measurements," *IEEE Transactions on Microwave Theory and Techniques*, vol. 67, no. 10, pp. 4042–4054, 2019.

[16] M. Yazgan, H. Arslan, and S. Vakalis, "High-Accuracy Indoor Ranging Using Microwave OFDM Signals," *IEEE Microwave and Wireless Technology Letters*, vol. 34, no. 12, pp. 1407–1410, 2024.

[17] S. Ding, B. Chen, J. Li, J. Yao, Y. Yuan, D. Jiang, and F. Qin, "Integrated Sensing and Communication: Prototype and Key Processing Algorithms," in *2023 IEEE International Conference on Communications Workshops (ICC Workshops)*, 2023, pp. 225–230.

[18] S. Mercier, D. Roque, and S. Bidon, "Study of the Target Self-Interference in a Low-Complexity OFDM-Based Radar Receiver," *IEEE Trans. on Aerosp. and Electr. Syst.*, vol. 55, no. 3, pp. 1200–1212, 2019.

[19] "NR; Base Station (BS) Radio Transmission and Reception (Release 15)," 3GPP, Tech. Rep. TS 38.104 v15.4.0, Apr. 2019.

[20] M. F. Keskin, M. M. Mojahedian, J. O. Lacruz, C. Marcus, O. Eriksson, A. Giorgetti, J. Widmer, and H. Wymeersch, "Fundamental Trade-Offs in Monostatic ISAC: A Holistic Investigation Towards 6G," *IEEE Transactions on Wireless Communications*, pp. 1–1, 2025.

[21] M. Braun, C. Sturm, and F. K. Jondral, "Maximum likelihood speed and distance estimation for OFDM radar," in *2010 IEEE Radar Conference*, 2010, pp. 256–261.

[22] Z. Zhang, X. Chai, K. Long, A. V. Vasilakos, and L. Hanzo, "Full duplex techniques for 5G networks: self-interference cancellation, protocol design, and relay selection," *IEEE Communications Magazine*, vol. 53, no. 5, pp. 128–137, 2015.

[23] E. Everett, A. Sahai, and A. Sabharwal, "Passive Self-Interference Suppression for Full-Duplex Infrastructure Nodes," *IEEE Transactions on Wireless Communications*, vol. 13, no. 2, pp. 680–694, 2014.

[24] E. Ahmed and A. M. Eltawil, "All-Digital Self-Interference Cancellation Technique for Full-Duplex Systems," *IEEE Transactions on Wireless Communications*, vol. 14, no. 7, pp. 3519–3532, 2015.

[25] J. Kim and N. Lee, "Adaptive Non-Linear Digital Self-Interference Cancellation for Full-Duplex Wireless Systems Using Ito-Hermite Polynomials," in *2018 ICC Workshops*, 2018, pp. 1–6.

[26] L. Ding, *Digital predistortion of power amplifiers for wireless applications*. Georgia Institute of Technology, 2004.

[27] "OpenAirInterface5G," accessed June 24, 2025. [Online]. Available: https://gitlab.eurecom.fr/oai/openairinterface5g